iScience

CellPress
OPEN ACCESS

Article

Flexible and scalable photothermal/electro thermal anti-icing/de-icing metamaterials for effective large-scale preparation

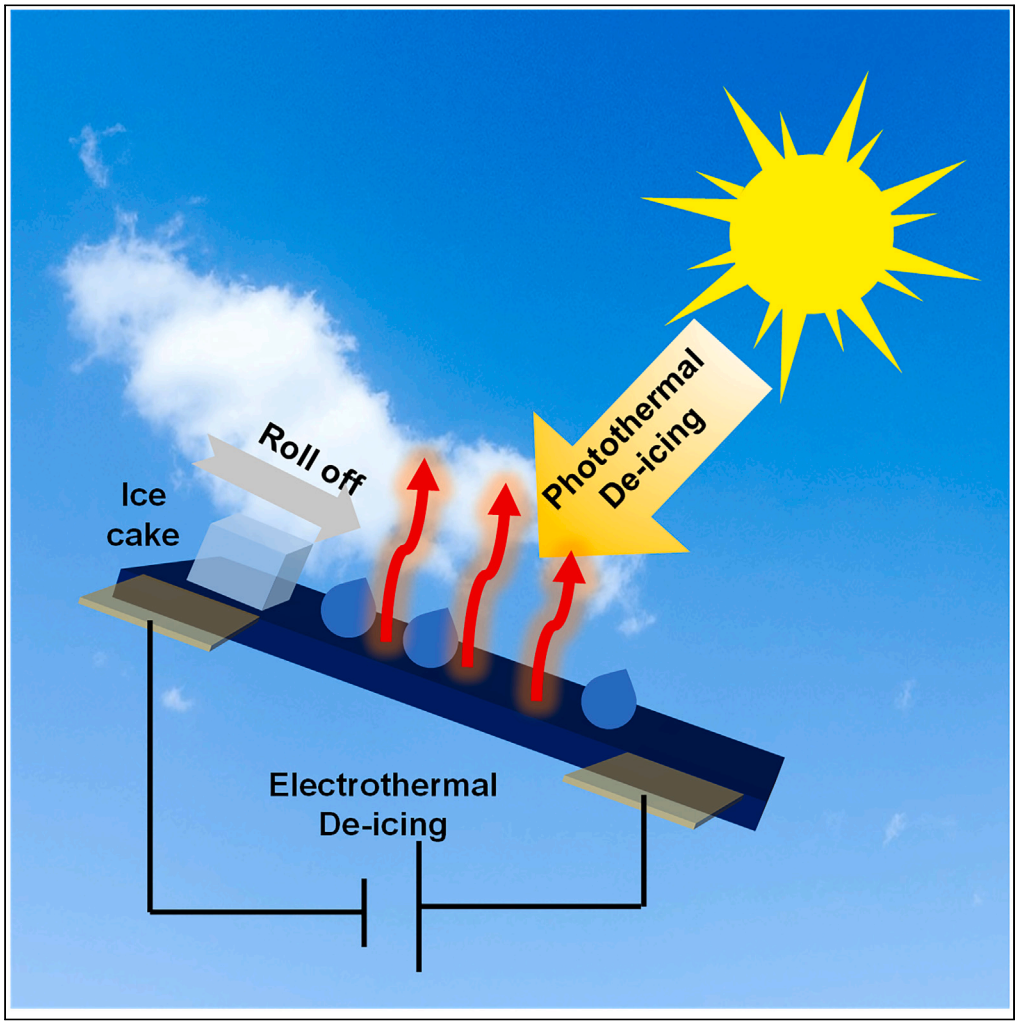

Tonghui Lu, Xianglin Li, Mengying Lu, ..., Zhe Liu, Shangzhen Xie, Song Lv

lvsong@whut.edu.cn

Highlights

This multifunctional superhydrophobic coating is low-cost, easy to produce, and scalable

The superhydrophobic coating delays icing significantly, achieving a 2500s delay at −20°C

The superhydrophobic coating has good electrothermal properties for fast de-icing at 1.6W

The superhydrophobic coating has excellent mechanical durability

Lu et al., iScience 27, 111086
November 15, 2024
https://doi.org/10.1016/j.isci.2024.111086

iScience

CellPress
OPEN ACCESS

Article

Flexible and scalable photothermal/electro thermal anti-icing/de-icing metamaterials for effective large-scale preparation

Tonghui Lu,[1] Xianglin Li,[1] Mengying Lu,[1] Wenhao Lv,[2] Wenzhuo Liu,[1] Xuanchen Dong,[1] Zhe Liu,[1] Shangzhen Xie,[3,4] and Song Lv[1,2,5,*]

SUMMARY

Anti-icing and de-icing are vital for infrastructure maintenance. While carbon-based materials with photothermal or electrothermal effects have advanced, they face challenges like environmental dependence, poor resistance, high energy consumption, and complex manufacturing. Here, we developed a scalable, hybrid metamaterial driven by photothermal/electrothermal for all-weather anti-icing/de-icing. Its nanostructured surface delays icing by 360 s at −30°C, breaking records across a wide temperature range. The porous structure enhances light absorption, achieving a delayed icing time of 2500 s at −20°C under one sunlight. The graphene film's high conductivity allows rapid de-icing with 1.6W power. After 720 h of outdoor exposure, the metamaterial retained a contact angle above 150°, confirming durability. More critically, we have demonstrated that the metamaterial can be manufactured on a large scale, which is essential for improving the economics of the anti-icing/de-icing sector.

INTRODUCTION

Icing presents significant economic and security challenges.[1–3] Water freezing is a widespread phenomenon that has implications in various fields, including climate, industry, and materials science.[4–6] There is an urgent need for more cost-effective de-icing methods as traditional methods, such as chemical treatment, mechanical de-icing, and thermal de-icing, have high energy consumption, low efficiency, and are prone to secondary pollution of the environment.[7–11] Fortunately, superhydrophobic materials,[12–14] and slippery liquid-infused porous surfaces (SLIPS)[15] have been extensively studied. Due to the reduced adhesion strength of ice on the material surface, the probability of surface ice formation is reduced, and the energy consumption for de-icing is reduced, making them have a certain anti-icing/de-icing effect.[16] For superhydrophobic materials, however, the interlocking of ice droplets and surfaces tends to occur during dynamic de-icing, thereby increasing ice adhesion strength.[17,18] For SLIPS, the lubricant in SLIPS is highly susceptible to depletion due to evaporation or capillary core inhalation into the ice structure, which reduces its de-icing performance.[19,20] In recent years, several photothermal materials have been used to efficiently convert solar energy into heat.[21,22] These materials are environmentally friendly and can effectively prevent ice nucleation.[23] However, photothermal de-icing is greatly affected by environmental conditions and weather, and cannot be utilized even at night without light, reducing the effectiveness and time economy of de-icing.[24]

Multifunctional anti-icing/de-icing materials with simultaneous superhydrophobic, photo-thermal, and electro-thermal properties are a growing trend that is highly attractive in terms of economy and efficiency.[25] To date, the efficiency of anti-icing/de-icing has been improved by multifunctional de-icing materials, reducing the uncontrollable impacts on the environment.[26,27] However, another issue worth noting is that the cost of synthetic materials (plasma materials,[28,29] magnetic particles[30,31]), and the complexity of laser etching technology,[32] LBL (Layer-by-Layer) assembly technology,[10] have been major constraints to the mass production of de-icing materials. For practical considerations, there is an urgent need for lightweight and durable synthetic materials that are scalable, portable, and easy to prepare on a large scale.

Carbon-based materials with excellent mechanical, electrical conductivity, thermal, and photothermal properties have been favored for the development of high-performance photothermal and electrothermal anti-icing/de-icing materials and devices.[33–35] Cross-scale carbon-based materials and devices using carbon-based materials (carbon particles, CNT/GNP doped nanocomposites, carbon fiber, carbon nanotubes [CNTs], and graphene nanosheets [GNPs]) assisted by nano-microfabrication techniques and the structure of the substrate materials have yielded excellent absorbance, directional thermal conductivity/electrical conductivity, thermal stability, corrosion resistance.[4,36,37] This means that the use of reusable cross-scale carbon-based materials for scalable and effective multifunctional anti-icing/de-icing has great

[1]School of Naval Architecture, Ocean and Energy Power Engineering, Wuhan University of Technology, Wuhan 430063, China
[2]School of Materials Science and Engineering, Wuhan University of Technology, Wuhan 430063, China
[3]School of Energy and Environment, City University of Hong Kong, Tat Chee Avenue, Kowloon Tong, Hong Kong, China
[4]Ministry of Education Key Laboratory for the Green Preparation and Application of Functional Materials, Hubei University, Wuhan 430062, China
[5]Lead contact
*Correspondence: lvsong@whut.edu.cn
https://doi.org/10.1016/j.isci.2024.111086

potential if manufacturing can be simplified, lightweight, flexible and scalable, and the range of applications can be extended to achieve perfect absorption, thermal, and electrical conductivity over a wide temperature range.

Here, we use multi-layer graphene assembly films and carbon nanoparticles to prepare lightweight and durable hybrid metamaterials that are scalable, portable, and easy to prepare on a large scale, demonstrating efficient all-weather active and passive anti-icing/de-icing. The metamaterial consists of a multilayer graphene assembly film and carbon nanoparticles encapsulated with PDMS (Supplementary Materials and Methods). The metamaterial synergistically matches the effects of photon multiple scattering and particle near-field radiation, which improves the ability of the composite particle cluster to capture solar radiation, and the full-spectrum solar energy absorption is as high as 98%, which is 2–3 times higher than that of the traditional photothermal conversion materials. Carbon nanoparticles with gaps as blackbodies exhibit high photothermal conversion efficiencies, with the surface temperature of the metamaterial increasing to 68.8°C under one sunlight. The delayed icing time of the metamaterial surface can reach an amazing 2500s under one sunlight. Because of the extraordinarily long delayed icing times at −10°C, −20°C, and −30°C, the metamaterial has broken the record for effective delayed icing effects over a wide temperature domain. Furthermore, multiple mechanical durability tests of metamaterials after 720 h of outdoor exposure have shown that the contact angle remains above 150°, making them lightweight and durable. The metamaterial (multilayer graphene-assembled film) is flexible, lightweight, highly electrically conductive, and has a high in-plane thermal conductivity, which is higher than most of the reported carbon nanotube and graphene materials. These advantages make the ultra-low-power electrically heated anti-icing/de-icing layer successful in a wide range of temperatures and even in extreme environments, which prompts the metamaterial to warm up to 85°C with only 0.25 w/cm^2 EPD, as well as rapid de-icing in 70 s at 0.2 w/cm^2 EPD. Furthermore, as a versatile and scalable material, it does not necessitate a flexible substrate, significantly streamlining the manufacturing process. Manufactured in 270 mm wide sheets at 3 m/min, the metamaterial is used in a wide range of applications in automotive, marine, aerospace, telecoms, power, energy, infrastructure, outdoor installations and instrumentation, particularly in carriers for irregularly curved surfaces of complex outdoor devices.

RESULTS

Preparation and characterization of the metamaterial

To achieve excellent mechanical properties, high electrical conductivity, and high thermal conductivity, we obtained highly flexible, foldable, and crack-free graphene films (GAFs) as substrates through high-temperature annealing and rolling processes of reduced graphene oxide (Figure S1). Taking this as the starting point, the graphene film is placed at two-thirds of the flame center of the candle, and the graphene film moves at a rate of 2 cm/s, so that the carbon nanoparticles generated by the incomplete combustion of the candle are uniformly adhered to the surface of the graphene film (Figure S1B). In addition, the generated carbon nanoparticles were immersed in a mixed solution of PDMS at a rate of 3 cm/s, which resulted in a tightly bound layer of carbon nanoparticles (Figure S1C). The source of carbon nanoparticles in this design is besides candles, carbon from biomass and fossil fuel combustion can be used as a source material for carbon nanoparticles[38] (Figure 1A).

Carbon nanoparticles are attached *in situ* to graphene films to serve as light absorbers at the top of the metamaterial and as electrothermal conductors at the bottom (Figure 1B). The light-absorbing layer consists mainly of carbon nanoparticles that form a porous structure, a 3D nanostructure that promotes light absorption by reducing reflections and lengthening the light path. Carbon nanoparticles have high broadband (300–2500nm) solar absorption properties and low transmittance/reflectance, resulting in high photothermal conversion efficiencies, with up to 98% absorption in the full spectral range of the metamaterial tested (Figure 1C). Furthermore, the material's high in-surface thermal conductivity enhances its resistance to changes in thermal response due to environmental factors such as light inhomogeneities caused by clouds, objects, and localized ice shading on certain parts of the surface object.[20] The high thermal conductivity of the graphene film (1273.8 $w \cdot m^{-1} \cdot k^{-1}$) in the heat diffusion layer promotes lateral heat diffusion, ensuring uniform heat distribution across the surface of the metamaterial. The metamaterial can be adhered to the surface of any object and has a wide range of applications.

Surface morphology and wettability of the metamaterial

As shown in Figures 2A–2C, the surface topography of graphene films, GCS (polymerization of graphene films with carbon nanoparticles), and GPCS is observable. The figure illustrates that the GCS surface has a random distribution of micro- and nanoscale cluster particle structures, while the surface of the graphene film is relatively smooth. The figure illustrates that the GCS surface has a random distribution of micro- and nanoscale cluster particle structures, while the surface of the graphene film is relatively smooth. The particles on the surface of GPCS are more rounded and have a larger diameter than those on GCS. This may be due to the connecting role of PDMS between the particles. As shown in Figures 2D and 2E, the XRD test results of graphene samples prepared by reactant graphene oxide and redox method are demonstrated, respectively. The figure shows that the position of the characteristic peaks of graphene prepared by the redox method has changed. This change in position is due to a decrease in the layer spacing of the graphene, as predicted by Bragg's formula. The XRD test results of GPCS are shown in Figure 2F. The characteristic diffraction peaks of GPCS remain almost unchanged compared to the graphene prepared by the redox method. The elemental distribution of GPCS is given in Figure 2G, demonstrating a uniform distribution of Si, C, and O elements in the surface structure and confirming the effectiveness of the sample preparation process.

CS is an excellent photothermal superhydrophobic material. The graphene film, prepared by the redox method, has excellent high-temperature resistance. However, the graphene film alone does not exhibit superhydrophobicity, as shown in Figure 2H, where its contact angle is only 115°. The graphene film was positioned at the two-thirds point of the candle flame. As a result, soot from the incompletely burnt candle gradually deposited onto the graphene film, forming a deposition layer structure as more and more tiny particles accumulated. The

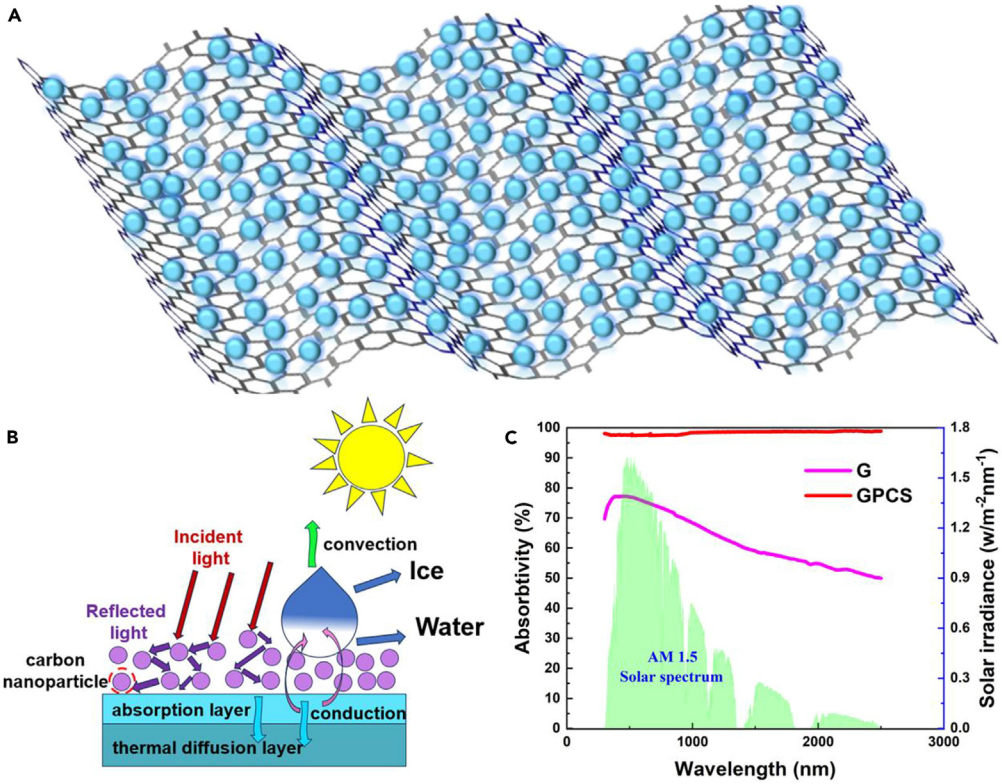

Figure 1. Graphene, carbon nanoparticle metamaterials

(A) Schematic representation of randomly distributed carbon nanoparticles adsorbed *in situ* on graphene film.

(B) Heat transfer mechanisms in the metamaterial consisting of light-absorbing and heat-diffusing layers, as well as analyses of light paths in micro- and nano-layered structures and heat transfer mechanisms in photo-thermal anti-icing materials at the microscopic level.

(C) The graphene film maintains an absorption of over 50% across the full wavelength range, while the GPCS maintains an absorption of approximately 98% over the same range.

sedimentary layer structure has a micro- and nano-scale roughness with low surface energy, consistent with Wenzel and Cassie-Baxter's model for good superhydrophobicity. A contact angle of 155° was measured using a contact angle meter in Figure 2I. However, the microstructure of the soot layer can be characterized by its porosity and looseness. This structure typically consists of small particles and fragments with weak interconnections, making them susceptible to fragmentation. To enhance the mechanical properties of the candle soot layer, it was immersed in a mixed solution of PDMS and 1H,1H,2H,2H-perfluorooctyltriethoxysilane (PFOTES). The PDMS polymer chains filled microporous structures during the coating process. The adhesion of the candle soot layer was enhanced by the treatment, and the surface energy of the CS was decreased by 1H,1H,2H,2H-perfluorooctyltriethoxysilane, resulting in further enhancement of the superhydrophobicity of the CS surface. The contact angle of the GPCS was measured to be 157° using a contact angle meter in Figure 2J.

Effect of CS thickness on photothermal conversion characteristics

The thickness of candle soot is adjusted by varying the deposition time. The optimum deposition thickness was determined by testing the photothermal conversion properties of candle soot at different deposition thicknesses. Figures 3A–3C show the cross-sectional views of the 45.9 μm, 49.7 μm, and 52.5 μm candle soot layers, respectively. The temperature rise (ΔT) of the CS was measured under one sunlight, and Figure 3D shows that the temperature of the surface of the three different thicknesses of the CS increased gradually with the enhancement of the illumination time. Meanwhile, when the CS thickness is 52.5 μm, the equilibrium temperature of the coated surface is able to reach 65°C under one sunlight, and its heating rate is able to reach 0.55°C/s, which is competitive with previously reported photothermal ice-removing surfaces. In addition, it can be concluded from Figure 3E that the temperature rise of the coating surface increases gradually with the increase of the CS thickness and tends to stabilize when the CS thickness is greater than 52.5 μm. This is mainly attributed to the effects of heat conduction and radiation from the soot layer. Once the soot layer reaches a certain thickness, it becomes a relatively good insulator, reducing the ability to conduct heat outwards through the soot layer. At this point, more heat is retained inside the soot layer than is conducted to the surface of the coating. Therefore, even if the candle continues to burn, the thicker the soot layer, the rate of increase in surface temperature rise slows down and eventually stabilizes.

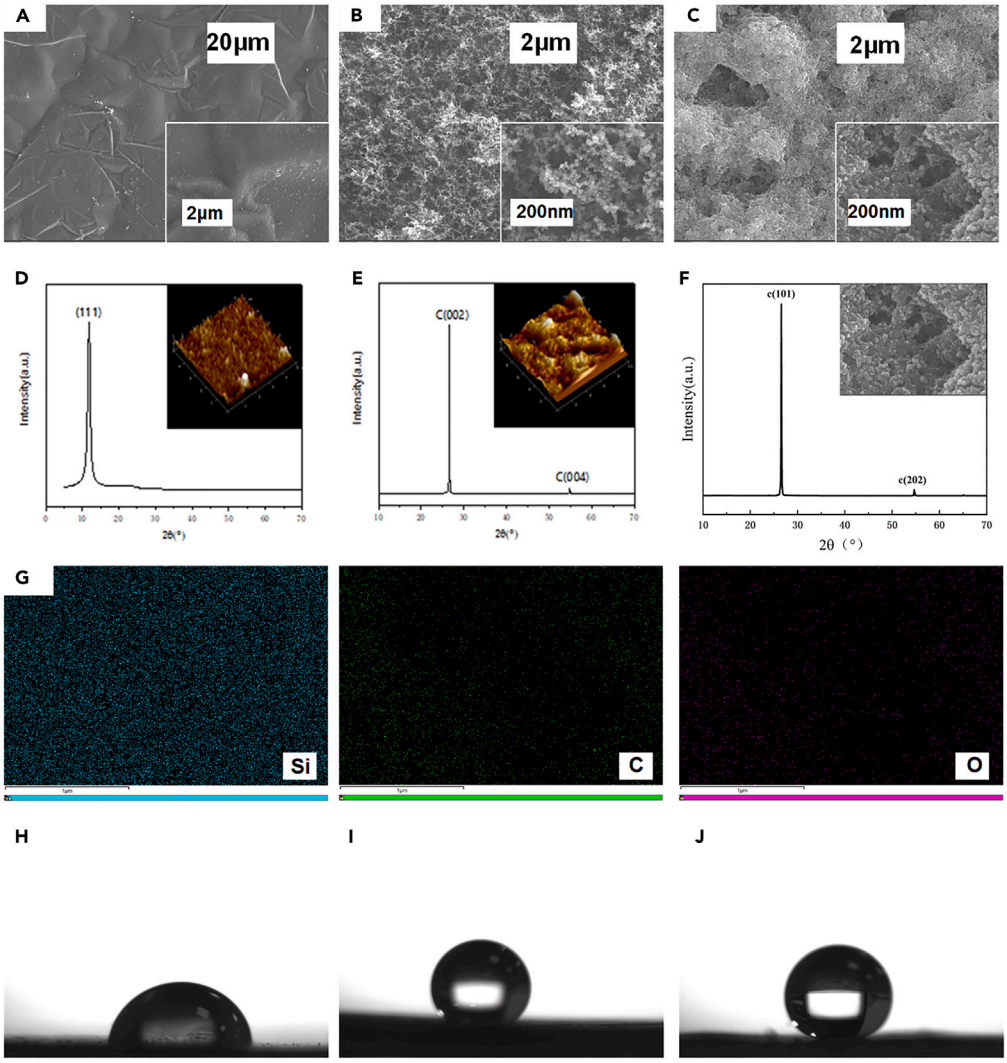

Figure 2. Surface characterization and wettability of the metamaterial

(A) The SEM characterization image of graphene film shows a relatively smooth surface.

(B) Carbon nanoparticles are *in situ* loaded onto the graphene film, and the microscopic morphology image of carbon nanoparticles reveals the formation of numerous clusters on the surface, aggregated at a scale of 200 nm.

(C) Morphology image of carbon nanoparticles after multiple coatings with PDMS mixed solution, showing a tight binding and smoother, more rounded particle morphology.

(D and E) XRD spectra of graphene films prepared by graphene oxide and reduced graphene oxide methods, respectively. The characteristic peak positions shift after the treatment of graphene oxide.

(F) XRD spectra of GPCS with almost unchanged characteristic peaks compared to graphene film.

(G) Elemental composition analysis of GPCS reveals its primary composition as Si, C, and O, with a higher content of Si.

(H–J) Contact angle test images of graphene film, GCS(polymerization of graphene films with carbon nanoparticles), and GPCS, indicating excellent superhydrophobicity in GPCS.

Testing of photothermal conversion properties of the metamaterial

To evaluate the photothermal conversion properties of the metamaterial, we tested their equilibrium temperatures at various optical power densities (OPD). When the metamaterials were exposed to different OPDs (0.1 w/cm^2, 0.15 w/cm^2, and 0.2 w/cm^2), the surface equilibrium temperature of the metamaterial increased gradually with the increase of OPD (Figure 4A). In addition, we recorded the infrared thermograms of the materials at different OPDs separately. The surface temperature of the metamaterial reaches different equilibrium values as the OPD varies: 67.7 °C at 0.1 w/cm^2, 85 °C at 0.15 w/cm^2, and 98.8 °C at 0.2 w/cm^2. Furthermore, we explored the temperature change of three different materials under one sunlight. Due to the low absorption of aluminum sheet in the full spectral range, the equilibrium temperature of the aluminum sheet at an OPD of 0.1 w/cm^2 is only about 40°C, whereas the metamaterial can reach 62°C (Figure 4B). These results

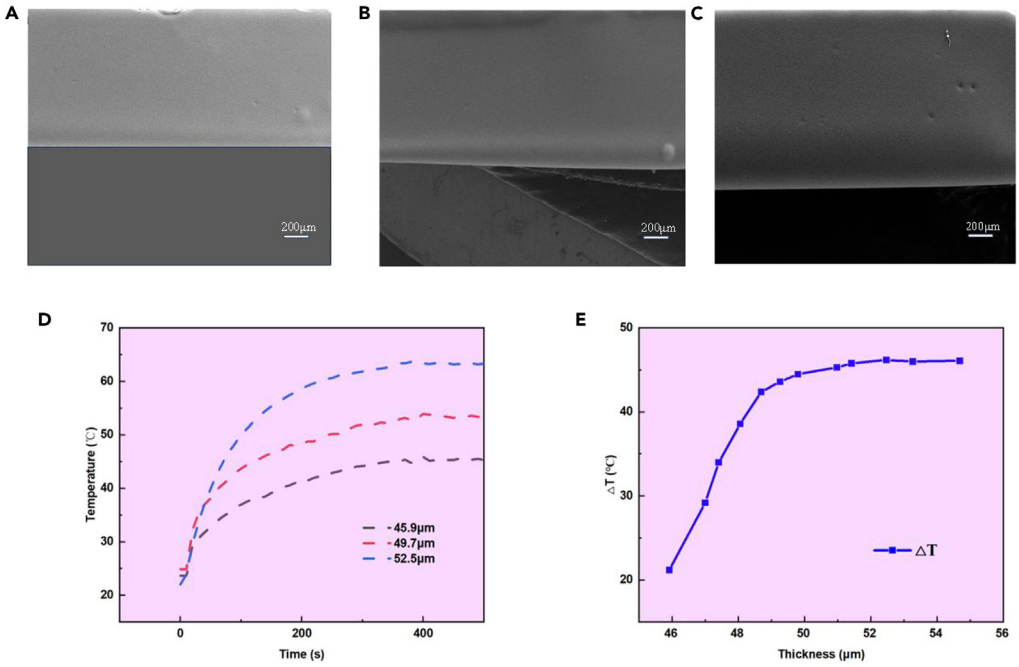

Figure 3. Effect of deposited CS layer thickness on photothermal conversion characteristics

(A–C) SEM images of CS cross sections with thicknesses of 45.9 μm (A), 49.7 μm (B) and 52.5 μm (C), respectively.

(D) Photothermal conversion characteristic curves of CS coatings with three different thicknesses.

(E) Temperature rise curves (ΔT) for different CS thicknesses in one sunlight.

demonstrate the superior photothermal conversion properties of the metamaterial. After switching off the solar simulator, the surface temperatures of the three materials decreased rapidly. The equilibrium temperatures of the three materials then converged after a while. It is worth noting that the superhydrophobic photothermal material exhibited the fastest rate of temperature drop. Furthermore, Figure 4C illustrates the cyclic temperature variation of the metamaterial at an OPD of 0.1w/cm^2. The results indicate that the metamaterial exhibits stable photothermal properties, with the maximum and minimum temperatures of the metamaterial essentially converging and the process curves remaining consistent throughout the five cyclic tests. This is crucial for the practical implementation of the metamaterial. In addition, by changing the shading area of the metamaterial and maintaining a light intensity of 0.1 w/cm^2, it can be found that the relative percentage temperature difference between the shaded and unshielded portions was only 0.128 for half the shaded area, and the relative percentage temperature difference gradually tends to zero as the shading area decreases (Figure 4E). It can be concluded that the metamaterial has a strong ability to resist environmental changes, especially solar irradiation, and has a significant resistance to the actual environment of clouds, shade, pollutants and other parts of the shade, highly adaptable to the environment. Furthermore, the delayed icing time under different OPDs was tested separately (Figure 4F), and the delayed icing time gradually became longer with the increase of OPD. Moreover, the defrosting time and de-icing time can reach 114 s and 450 s, respectively under the light intensity of 0.1 w/cm^2 (Figure S6).

Electrothermal property testing of the metamaterial and electrothermal de-icing performance

Although photothermal de-icing can remove ice from a material's surface under certain conditions, it is not effective in wet, dark, and cold environments.[39] In such cases, proactive intervention with electrical de-icing is necessary. After testing, the graphene film exhibited an electrical conductivity of up to 1.13 × 10^6 m/s (Figure S5), forming the basis for metamaterial electrothermal de-icing. The entire electrical heating system relies heavily on the electrical properties of the metamaterial.

The electrothermal properties of the metamaterials can be studied at different electrical heating power densities (EPD). The results indicate that the temperature of the metamaterial surface increases with an increase in EPD, and the equilibrium temperature changes of the EPD and the metamaterial are synchronized, which is by Joule's law. The surface temperature of the metamaterial reaches only 49.3 °C at an EPD of 0.1 w/cm^2, but can reach 82.6°C when the EPD is increased to 0.25 w/cm^2 (Figure 5A). This demonstrates the metamaterial's strong electrothermal properties. The figure illustrates the metamaterial's rapid electro-thermal response, with the surface reaching equilibrium temperature quickly. As shown in Figure 5B, it primarily illustrates the temperature variation of the metamaterial under different EPDs during heating and cooling cycles, while Figure 5C illustrates the temperature variation of the metamaterial under the same EPD during heating/cooling cycles. The results indicate that the maximum and minimum temperatures of the metamaterials under the same EPD are essentially identical, leading to the conclusion that the metamaterials possess electro-thermal stabilization properties. Additionally, infrared thermograms were taken of the metamaterial at various EPDs (Figure S7). The results indicate that the surface temperature of the metamaterial is uniformly

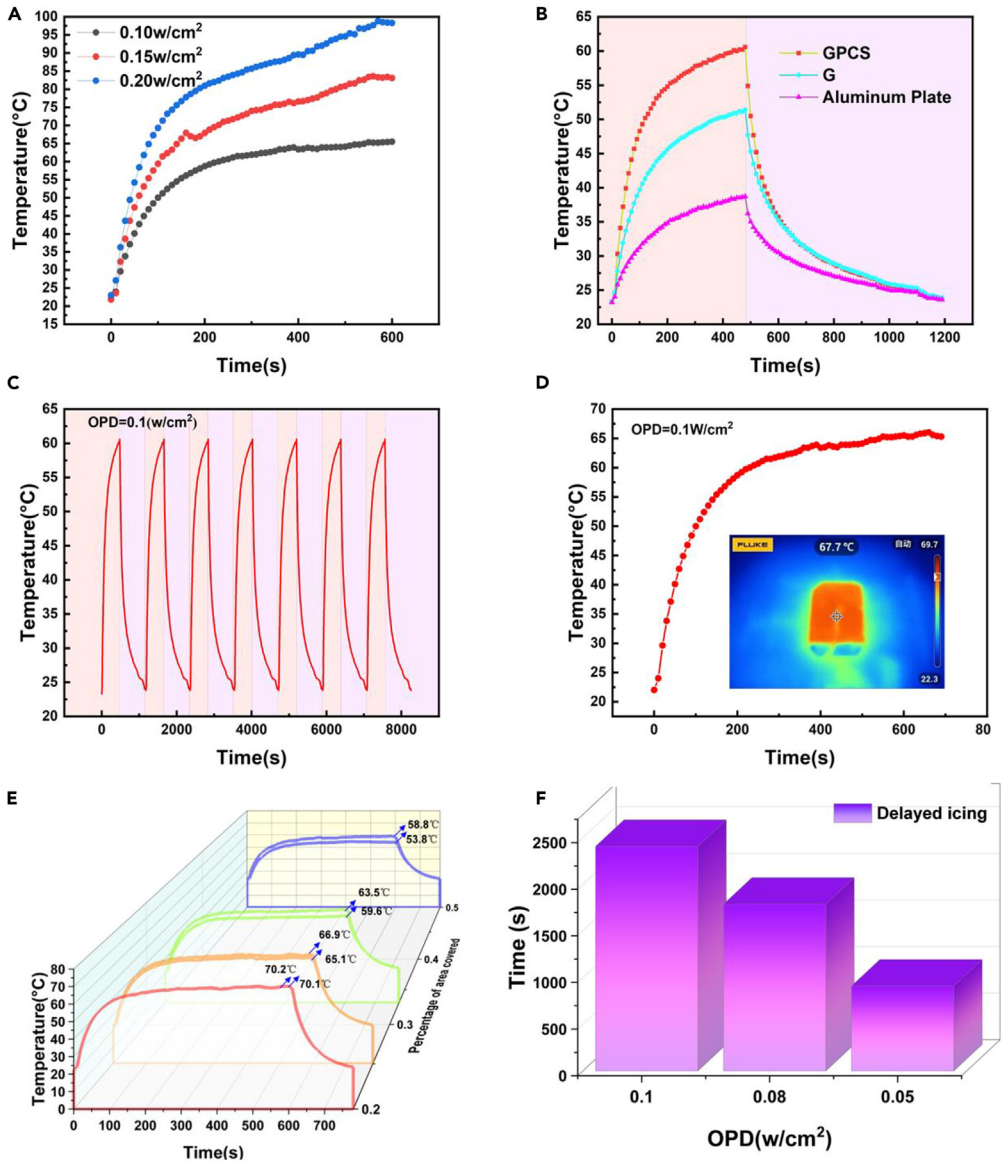

Figure 4. Photothermal conversion property testing

(A) Demonstration of the equilibrium temperature of the metamaterial at three different OPDs.

(B) The photothermal response of different materials to individual sunlight was tested under ambient conditions with lights on and off.

(C) The photo-thermal stability of the metamaterial was tested under cyclic on and off light ambient conditions.

(D) The temperature variation of the metamaterial under individual sunlight, and Schematic thermal imaging of equilibrium temperatures.

(E) Effect of masking area on the heat transfer of the metamaterial.

(F) Delayed icing test of the metamaterial at different OPDs.

distributed and gradually increases with the increase of EPD. The temperature at the edge of the metamaterial is relatively low, mainly because the contact area with the air at the edge is larger and the convective heat transfer is stronger, resulting in greater heat loss. In addition, the metamaterial easily removes surface ice with only 1.6W of output power (Figure S7). This work provides a new direction for the preparation of ultralow power de-icing/anti-icing as well as for the development of flexible and energy-efficient de-icing/anti-icing materials.[40]

Testing of the metamaterial for delayed icing property

Ice-phobicity is a key indicator of the anti-icing performance of the material surfaces. The metamaterial improves the ice-phobic properties of material surfaces by preventing adhesion under the impact of water droplets,[41–43] inhibiting heat transfer during the icing process,[44,45] and decreasing ice adhesion,[46] which are three aspects of ice-phobicity.

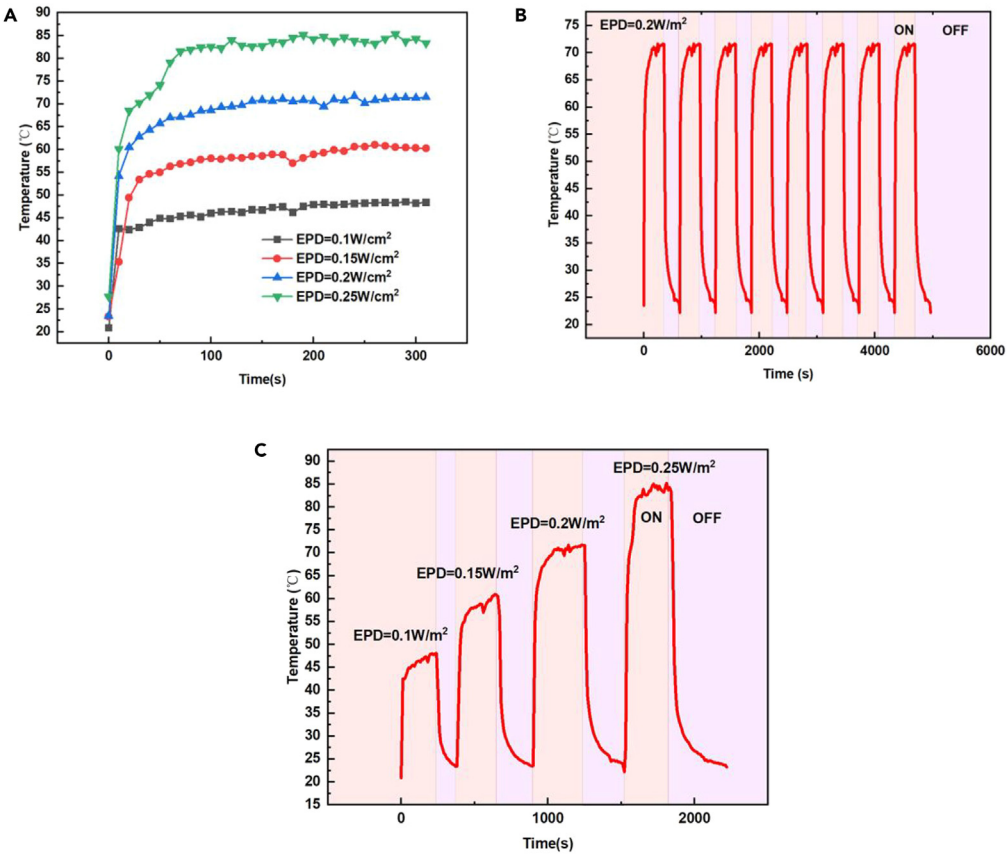

Figure 5. Electrothermal property testing of the metamaterial

(A) The electro-thermal response of the metamaterial at different EPDs.

(B) Testing the electro-thermal stability properties of the metamaterial under multiple switching power conditions.

(C) Testing the electro-thermal response of the metamaterial under switching power supply conditions with gradually increasing EPDs.

To assess the delayed icing properties of the metamaterial, we recorded the delayed icing conditions of the droplets. The metamaterials were tested at −10°C, −20°C, and −30°C and 35% ± 5% relative humidity (Figure 6A). As shown in Figure 6A, this indicates that a 10μL droplet placed on the metamaterial will assume a spherical shape due to the superhydrophobic properties. After 360 s, the droplet begins to freeze and eventually freezes completely within 400 s, forming a spike shape at the top. Droplet condensation nucleation is dependent on the free energy of the substrate surface and the wettability of the metamaterial surface. By reducing the wettability of the metamaterial surface, the free energy of the interface can be reduced, thereby achieving delayed icing. More critically, the explanation for this phenomenon can be attributed to the interfacial geometry of the metamaterial surface. The metamaterial has micro- and nano-scale rough structures that can trap air with relatively low thermal conductivity.[47] This reduces the thermal conductivity of the droplets to the solid surface, thereby slowing down the icing time of the droplets. As the temperature rises to −20°C, the delayed icing time increases to nearly 812 s, and as the temperature continues to rise to −10°C, the delayed icing time can increase to an astounding 1200 s. It is evident that as the refrigeration plate cooling temperature increases, the delayed icing time also increases.

In order to gain a clearer understanding of the delayed icing capability of the metamaterial, we have investigated, studied, and compared the delayed icing properties of some of the materials described in the literature. The results revealed that the metamaterial composed of carbon nanoparticles and graphene film demonstrated outstanding performance in delaying ice formation (Figure 6B). In addition, the use of graphene film as a base material for anti-icing/de-icing has the advantage that its weight is easy to laminate on curved surfaces, and its good flexibility and mechanical properties allow it to be adapted to any curved surface. However, one of the most compelling advantages of developing graphene film-carbon nanoparticle hybrid metamaterials is the possibility of low-cost, scalable fabrication. We successfully produced a set of 270 mm wide metamaterial films at a speed of 3 m/min (Figure 6C).

Mechanical durability testing

The metamaterial's robustness is crucial for protecting the material. The sample's contact and roll angles were tested once per 20g drop while varying the amount of sand dripped. The flowchart of the experimental setup is shown in Figure 7A. As shown in Figure 7B, after the

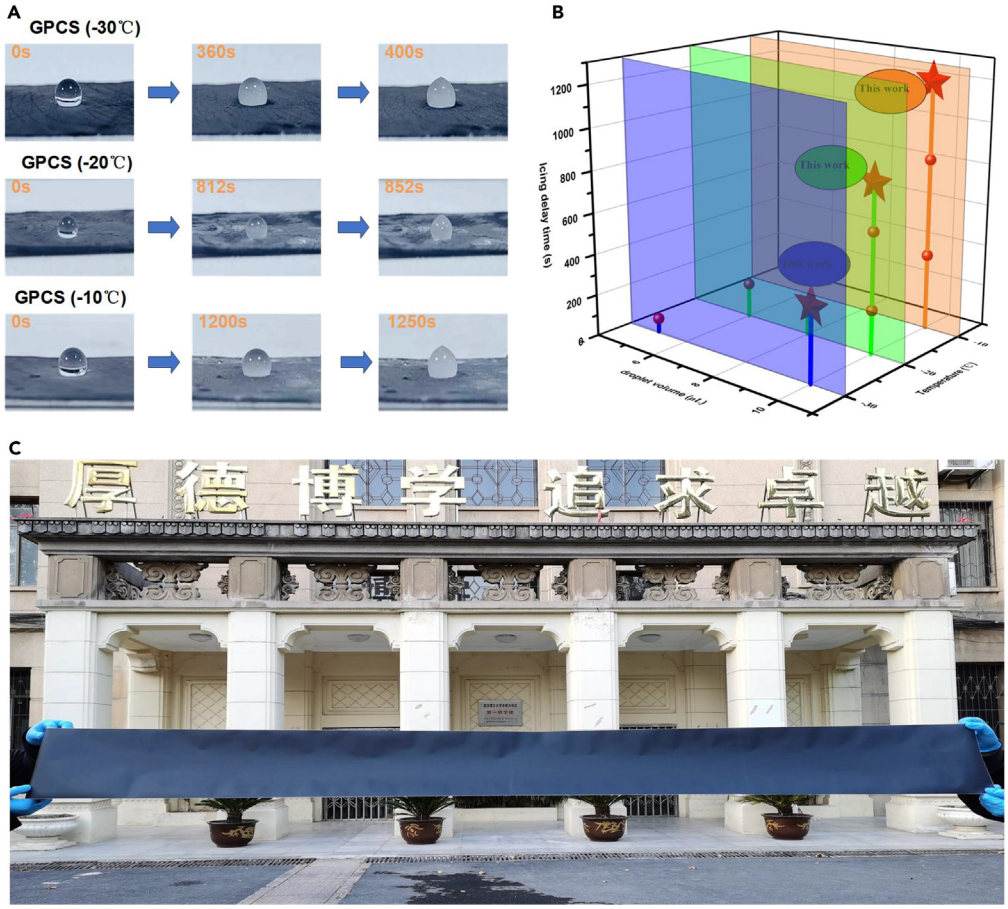

Figure 6. Testing the delayed icing of metamaterials in various environments and conditions

(A) The delayed icing condition of the metamaterial was tested separately in different environments.

(B) Comparison of the delayed icing properties of metamaterials with those of other materials mentioned in the literature.

(C) Photograph of a set of 270 m wide hybrid metamaterial films produced at 3 m/min.

metamaterial was impacted by the sand, the contact angle of its surface underwent a slight decrease, but the overall contact angle remained above 150°, and the rolling angle increased slightly, but the overall increase was not very large. Similarly, the volume of the droplet was varied, and the contact angle and roll angle of the coated surface were tested after each 500mL drop. The flow of the device for droplet dropping (Figure 7C) is similar to that of Figure 7A. As shown in Figure 7D, it demonstrates that the surface's contact and rolling angles remained largely unchanged after being impacted by water droplets. These experiments lead to the conclusion that the metamaterial exhibits good mechanical durability. Moreover, through outdoor testing experiments, the contact angle of the metamaterial can still be maintained above 150° when placed in an outdoor environment for 720 h, demonstrating continuous durability.

DISCUSSION

In this study, we have prepared a novel metamaterial with a combination of flexible, photothermal-electrothermal properties, and strong superhydrophobicity for anti-icing and de-icing. Superhydrophobic materials with both active and passive de-icing were prepared by *in situ* loading of carbon nanoparticles on graphene membranes and encapsulation with PDMS. The metamaterial exhibits excellent photothermal and electrothermal properties, reaching a surface temperature of 67.7°C under a single sunbeam, in addition to easily removing ice from the surface of the metamaterial at an output power of only 1.6w. The surface of the metamaterial is superhydrophobic with a water contact angle of 156°, and the CA of the metamaterial is still greater than 150° after water droplet impact and sand impact tests, demonstrating good superhydrophobic durability. The photo-/electro-thermal effect of the metamaterial gives the surface good active anti-icing capabilities when photo-heat and electricity are applied. This metamaterial combines active photo-/electro-thermal, passive superhydrophobicity to make the best use of heat for low-energy anti-icing and all-weather anti-icing capabilities. In addition, through the 720 h outdoor environment test, its contact angle can still be maintained at more than 150°, showing good mechanical durability. More importantly, the metamaterial is ready for

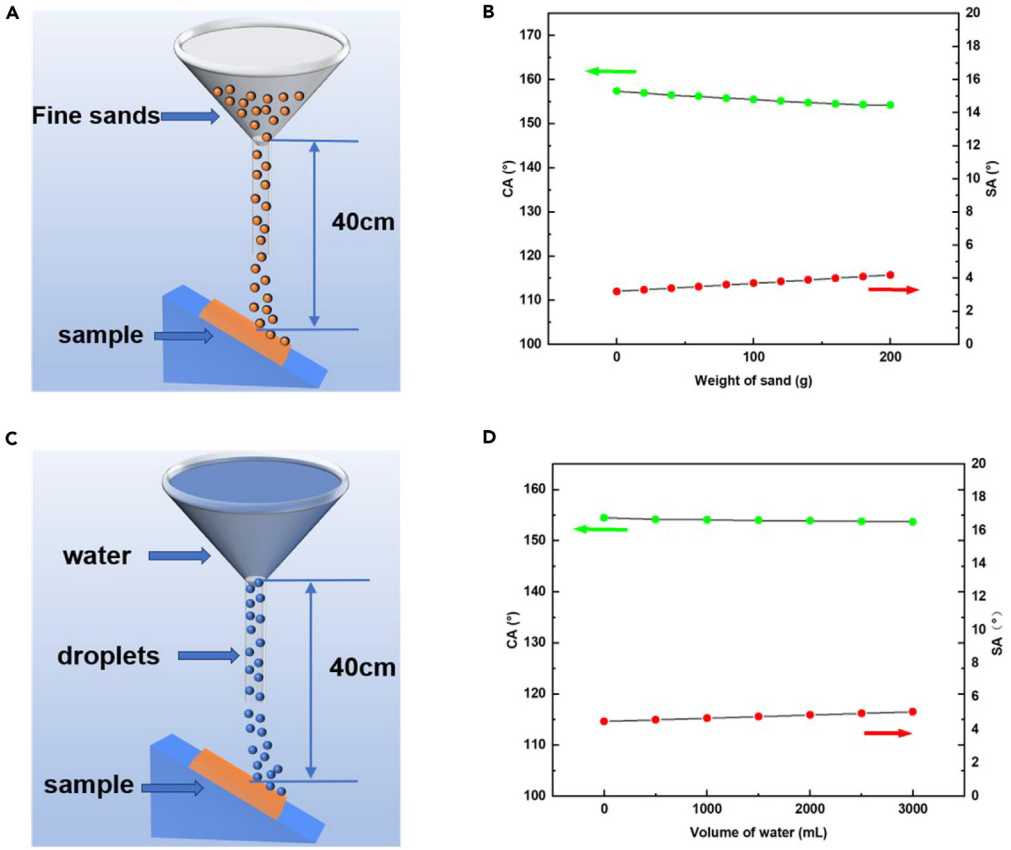

Figure 7. Mechanical durability testing of the metamaterial

(A and B) Continuous dropping of sand onto the inclined sample surface, maintaining a contact angle consistently above 150°, and a rolling angle consistently below 10°.

(C and D) The continuous dropping of liquid droplets onto the sample surface, with the contact angle consistently above 150° and the rolling angle consistently below 10°.

mass production, showing strong application potential. This study provides a promising way to achieve high efficiency in anti-icing/de-icing systems for aircraft, high-speed railways, and wind power generation.

Limitations of the study

1. Difference between experimental conditions and actual application environment: The conditions used in experiments, such as temperature, humidity and light intensity, are often carried out in the laboratory and cannot fully simulate the complex and changing environment in reality. For example, under a variety of extreme conditions such as low outdoor temperatures, wind and snow, and high humidity, the actual performance of the material may not be able to achieve the results in the experiment. Therefore, the performance and stability of materials in real environments still need to be further verified.
2. Long-term durability and environmental adaptability: The durability and stability of materials, particularly with regard to the decay of properties under long-term exposure to extreme weather conditions (e.g., strong winds, freeze-thaw cycles, etc.), has not been fully investigated. The mechanical and chemical stability of the material under these conditions, as well as the ability to maintain the superhydrophobic properties of the surface over the long term, still need to be assessed through longer-term outdoor experiments.

RESOURCE AVAILABILITY

Lead contact

Requests for further information and resources should be directed to the lead contact, Lv Song (lvsong@whut.edu.cn).

Material availability

This study did not generate new unique reagents.

Data and code availability

- All data can be obtained from the lead contact, provided the request is reasonable.
- The code related to the developed model can be accessed by reaching out to the lead contact.
- Any additional information required to reanalyze the data reported in this paper is available from the lead contact upon request.

ACKNOWLEDGMENTS

Funding: This study was sponsored by the National Natural Science Foundation of China (NSFC 52106268) and Nature Science Foundation of Hubei Province (2022CFB316).

AUTHOR CONTRIBUTIONS

T.L., X.L., and M.L.: substantial contributions to the conception or design of the work; or the acquisition, analysis, or interpretation of data for the work; W. Liu, W. Lv, X.D., and Z.L.: drafting the work or revising it critically for important intellectual content; S.L.: supervised the project. All authors read and commented on the manuscript.

DECLARATION OF INTERESTS

The authors declare no conflict of interest.

STAR★METHODS

Detailed methods are provided in the online version of this paper and include the following:

- KEY RESOURCES TABLE
- EXPERIMENTAL MODEL AND STUDY PARTICIPANT DETAILS
- METHOD DETAILS
  - Materials
  - Preparation of the metamaterial
  - Sample characterization
  - Performance evaluation
- QUANTIFICATION AND STATISTICAL ANALYSIS

SUPPLEMENTAL INFORMATION

Supplemental information can be found online at https://doi.org/10.1016/j.isci.2024.111086.

Received: July 22, 2024
Revised: August 28, 2024
Accepted: September 27, 2024
Published: October 10, 2024

REFERENCES

1. Golovin, K., Dhyani, A., Thouless, M.D., and Tuteja, A. (2019). Low–interfacial toughness materials for effective large-scale deicing. Science *364*, 371–375. https://doi.org/10.1126/science.aav1266.
2. Golovin, K., and Tuteja, A. (2017). A predictive framework for the design and fabrication of icephobic polymers. Sci. Adv. *3*, e1701617. https://doi.org/10.1126/sciadv.1701617.
3. Lv, J., Song, Y., Jiang, L., and Wang, J. (2014). Bio-Inspired Strategies for Anti-Icing. ACS Nano *8*, 3152–3169. https://doi.org/10.1021/nn406522n.
4. Bai, G., Gao, D., Liu, Z., Zhou, X., and Wang, J. (2019). Probing the critical nucleus size for ice formation with graphene oxide nanosheets. Nature *576*, 437–441. https://doi.org/10.1038/s41586-019-1827-6.
5. Jiang, J., Shen, Y., Wang, Z., Tao, J., Liu, W., Chen, H., Liu, S., Xie, X., and Zeng, C. (2022). Anti/de-icing performance of the one-step electrodeposited superhydrophobic surfaces: Role of surface polarity regulated by hydrocarbon radical length. Chem. Eng. J. *431*, 133276. https://doi.org/10.1016/j.cej.2021.133276.
6. Zhang, L., Gao, C., Zhong, L., Zhu, L., Chen, H., Hou, Y., and Zheng, Y. (2022). Robust photothermal superhydrophobic coatings with dual-size micro/nano structure enhance anti-/de-icing and chemical resistance properties. Chem. Eng. J. *446*, 137461. https://doi.org/10.1016/j.cej.2022.137461.
7. Azimi Dijvejin, Z., Jain, M.C., Kozak, R., Zarifi, M.H., and Golovin, K. (2022). Smart low interfacial toughness coatings for on-demand de-icing without melting. Nat. Commun. *13*, 5119. https://doi.org/10.1038/s41467-022-32852-6.
8. Chen, J., Luo, Z., An, R., Marklund, P., Björling, M., and Shi, Y. (2022). Novel intrinsic self-healing poly-silicone-urea with super-low ice adhesion strength. Small *18*, 2270112. https://doi.org/10.1002/smll.202270112.
9. Wong, T.-S., Kang, S.H., Tang, S.K.Y., Smythe, E.J., Hatton, B.D., Grinthal, A., and Aizenberg, J. (2011). Bioinspired self-repairing slippery surfaces with pressure-stable omniphobicity. Nature *477*, 443–447. https://doi.org/10.1038/nature10447.
10. Niu, W., Chen, G.Y., Xu, H., Liu, X., and Sun, J. (2022). Highly Transparent and Self-Healable Solar Thermal Anti-/Deicing Surfaces: When Ultrathin MXene Multilayers Marry a Solid Slippery Self-Cleaning Coating. Adv. Mater. *34*, 2108232. https://doi.org/10.1002/adma.202108232.
11. Bartels-Rausch, T. (2013). Ten things we need to know about ice and snow. Nature *494*, 27–29. https://doi.org/10.1038/494027a.
12. Gu, W., Li, W., Zhang, Y., Xia, Y., Wang, Q., Wang, W., Liu, P., Yu, X., He, H., Liang, C., et al. (2023). Ultra-durable superhydrophobic cellular coatings. Nat. Commun. *14*, 5953. https://doi.org/10.1038/s41467-023-41675-y.
13. Xu, L.H., Li, S.H., Mao, H., Li, Y., Zhang, A.S., Wang, S., Liu, W.M., Lv, J., Wang, T., Cai, W.W., et al. (2022). Highly flexible and superhydrophobic MOF nanosheet membrane for ultrafast alcohol-water separation. Science *378*, 308–313. https://doi.org/10.1126/science.abo5680.
14. Chu, F., Hu, Z., Feng, Y., Lai, N.C., Wu, X., and Wang, R. (2024). Advanced Anti-Icing Strategies and Technologies by Macrostructured Photothermal Storage Superhydrophobic Surfaces. Adv. Mater. *36*, e2402897. https://doi.org/10.1002/adma.202402897.
15. Pan, W., Wang, Q., Ma, J., Xu, W., Sun, J., Liu, X., and Song, J. (2023). Solid-Like Slippery Coating with Highly Comprehensive

Performance. Adv. Funct. Mater. *33*, 2302311. https://doi.org/10.1002/adfm.202302311.
16. Shi, J., Ke, S., Wang, F., Wang, W., and Wang, C. (2024). Recent advances in photothermal anti-/de-icing materials. Chem. Eng. J. *481*, 148265. https://doi.org/10.1016/j.cej.2023.148265.
17. Meuler, A.J., McKinley, G.H., and Cohen, R.E. (2010). Exploiting Topographical Texture To Impart Icephobicity. ACS Nano *4*, 7048–7052. https://doi.org/10.1021/nn103214q.
18. Sun, W., Wei, Y., Feng, Y., and Chu, F. (2024). Anti-icing and deicing characteristics of photothermal superhydrophobic surfaces based on metal nanoparticles and carbon nanotube materials. Energy *286*, 129656. https://doi.org/10.1016/j.energy.2023.129656.
19. Han, G., Nguyen, T.-B., Park, S., Jung, Y., Lee, J., and Lim, H. (2020). Moth-Eye Mimicking Solid Slippery Glass Surface with Icephobicity, Transparency, and Self-Healing. ACS Nano *14*, 10198–10209. https://doi.org/10.1021/acsnano.0c03463.
20. Dash, S., de Ruiter, J., and Varanasi, K.K. (2018). Photothermal trap utilizing solar illumination for ice mitigation. Sci. Adv. *4*, eaat0127. https://doi.org/10.1126/sciadv.aat0127.
21. Zhang, H., Zhao, G., Wu, S., Alsaid, Y., Zhao, W., Yan, X., Liu, L., Zou, G., Lv, J., He, X., et al. (2021). Solar anti-icing surface with enhanced condensate self-removing at extreme environmental conditions. Proc. Natl. Acad. Sci. USA *118*, e2100978118. https://doi.org/10.1073/pnas.2100978118.
22. Pyeon, J., Park, S.M., Kim, J., Kim, J.H., Yoon, Y.J., Yoon, D.K., and Kim, H. (2023). Plasmonic metasurfaces of cellulose nanocrystal matrices with quadrants of aligned gold nanorods for photothermal anti-icing. Nat. Commun. *14*, 8096. https://doi.org/10.1038/s41467-023-43511-9.
23. Zhang, L., Luo, B., Fu, K., Gao, C., Han, X., Zhou, M., Zhang, T., Zhong, L., Hou, Y., and Zheng, Y. (2023). Highly Efficient Photothermal Icephobic/de-Icing MOF-Based Micro and Nanostructured Surface. Adv. Sci. *10*, 2304187. https://doi.org/10.1002/advs.202304187.
24. Li, Z., Tian, Q., Xu, J., Sun, S., Cheng, Y., Qiu, F., and Zhang, T. (2021). Easily Fabricated Low-Energy Consumption Joule-Heated Superhydrophobic Foam for Fast Cleanup of Viscous Crude Oil Spills. ACS Appl. Mater. Interfaces *13*, 51652–51660. https://doi.org/10.1021/acsami.1c13574.
25. He, Z., Wu, C., Hua, M., Wu, S., Wu, D., Zhu, X., Wang, J., and He, X. (2020). Bioinspired Multifunctional Anti-icing Hydrogel. Matter *2*, 723–734. https://doi.org/10.1016/j.matt.2019.12.017.
26. Lin, C., Ma, W., Zhang, Y., Law, M.K., Li, C.Y., Li, Y., Chen, Z., Li, K., Li, M., Zheng, J., et al. (2023). A Highly Transparent Photo-Electro-Thermal Film with Broadband Selectivity for All-Day Anti-/De-Icing. Small *19*, 2301723. https://doi.org/10.1002/smll.202301723.
27. Li, B., Wu, N., Wu, Q., Yang, Y., Pan, F., Liu, W., Liu, J., and Zeng, Z. (2023). From "100%" Utilization of MAX/MXene to Direct Engineering of Wearable, Multifunctional E-Textiles in Extreme Environments. Adv. Funct. Mater. *33*, 2307301. https://doi.org/10.1002/adfm.202307301.
28. Mitridis, E., Schutzius, T.M., Sicher, A., Hail, C.U., Eghlidi, H., and Poulikakos, D. (2018). Metasurfaces Leveraging Solar Energy for Icephobicity. ACS Nano *12*, 7009–7017. https://doi.org/10.1021/acsnano.8b02719.
29. Richardson, H.H., Hickman, Z.N., Govorov, A.O., Thomas, A.C., Zhang, W., and Kordesch, M.E. (2006). Thermooptical Properties of Gold Nanoparticles Embedded in Ice: Characterization of Heat Generation and Melting. Nano Lett. *6*, 783–788. https://doi.org/10.1021/nl060105l.
30. Yin, X., Zhang, Y., Wang, D., Liu, Z., Liu, Y., Pei, X., Yu, B., and Zhou, F. (2015). Integration of Self-Lubrication and Near-Infrared Photothermogenesis for Excellent Anti-Icing/Deicing Performance. Adv. Funct. Mater. *25*, 4237–4245. https://doi.org/10.1002/adfm.201501101.
31. Gong, C., and Zhang, X. (2019). Two-dimensional magnetic crystals and emergent heterostructure devices. Science *363*, eaav4450. https://doi.org/10.1126/science.aav4450.
32. Murphy, R.J., and Ritter, G.J. (1966). Laser-induced Thermal Etching of Metal and Semiconductor Surfaces. Nature *210*, 191–192. https://doi.org/10.1038/210191a0.
33. Geim, A.K. (2009). Graphene: Status and Prospects. Science *324*, 1530–1534. https://doi.org/10.1126/science.1158877.
34. Xin, G., Yao, T., Sun, H., Scott, S.M., Shao, D., Wang, G., and Lian, J. (2015). Highly thermally conductive and mechanically strong graphene fibers. Science *349*, 1083–1087. https://doi.org/10.1126/science.aaa6502.
35. Basko, D. (2011). A photothermoelectric effect in graphene. Science *334*, 610–611. https://doi.org/10.1126/science.1214560.
36. Bai, Y., Yue, H., Wang, J., Shen, B., Sun, S., Wang, S., Wang, H., Li, X., Xu, Z., Zhang, R., and Wei, F. (2020). Super-durable ultralong carbon nanotubes. Science *369*, 1104–1106. https://doi.org/10.1126/science.aay5220.
37. Wang, H., Sun, X., Wang, Y., Li, K., Wang, J., Dai, X., Chen, B., Chong, D., Zhang, L., and Yan, J. (2023). Acid enhanced zipping effect to densify MWCNT packing for multifunctional MWCNT films with ultra-high electrical conductivity. Nat. Commun. *14*, 380. https://doi.org/10.1038/s41467-023-36082-2.
38. McConnell, J.R., Edwards, R., Kok, G.L., Flanner, M.G., Zender, C.S., Saltzman, E.S., Banta, J.R., Pasteris, D.R., Carter, M.M., and Kahl, J.D.W. (2007). 20th-Century Industrial Black Carbon Emissions Altered Arctic Climate Forcing. Science *317*, 1381–1384. https://doi.org/10.1126/science.1144856.
39. Wu, X., Lei, Y., Li, S., Huang, J., Teng, L., Chen, Z., and Lai, Y. (2021). Photothermal and Joule heating-assisted thermal management sponge for efficient cleanup of highly viscous crude oil. J. Hazard Mater. *403*, 124090. https://doi.org/10.1016/j.jhazmat.2020.124090.
40. Ba, H., Truong-Phuoc, L., Romero, T., Sutter, C., Nhut, J.-M., Schlatter, G., Giambastiani, G., and Pham-Huu, C. (2021). Lightweight, few-layer graphene composites with improved electro-thermal properties as efficient heating devices for de-icing applications. Carbon *182*, 655–668. https://doi.org/10.1016/j.carbon.2021.06.041.
41. Yang, C., Zeng, Q., Huang, J., and Guo, Z. (2022). Droplet manipulation on superhydrophobic surfaces based on external stimulation: A review. Adv. Colloid Interface Sci. *306*, 102724. https://doi.org/10.1016/j.cis.2022.102724.
42. Hu, S., Cao, X., Reddyhoff, T., Puhan, D., Vladescu, S.-C., Wang, J., Shi, X., Peng, Z., deMello, A.J., and Dini, D. (2020). Liquid repellency enhancement through flexible microstructures. Sci. Adv. *6*, eaba9721. https://doi.org/10.1126/sciadv.aba9721.
43. Liu, Y., Moevius, L., Xu, X., Qian, T., Yeomans, J.M., and Wang, Z. (2014). Pancake bouncing on superhydrophobic surfaces. Nat. Phys. *10*, 515–519. https://doi.org/10.1038/nphys2980.
44. Nosonovsky, M., and Hejazi, V. (2012). Why Superhydrophobic Surfaces Are Not Always Icephobic. ACS Nano *6*, 8488–8491. https://doi.org/10.1021/nn302138r.
45. Wang, L., Gong, Q., Zhan, S., Jiang, L., and Zheng, Y. (2016). Robust Anti-Icing Performance of a Flexible Superhydrophobic Surface. Adv. Mater. *28*, 7729–7735. https://doi.org/10.1002/adma.201602480.
46. Golovin, K., Kobaku, S.P.R., Lee, D.H., DiLoreto, E.T., Mabry, J.M., and Tuteja, A. (2016). Designing durable icephobic surfaces. Sci. Adv. *2*, e1501496. https://doi.org/10.1126/sciadv.1501496.
47. Mehanna, Y.A., Sadler, E., Upton, R.L., Kempchinsky, A.G., Lu, Y., and Crick, C.R. (2021). The challenges, achievements and applications of submersible superhydrophobic materials. Chem. Soc. Rev. *50*, 6569–6612. https://doi.org/10.1039/d0cs01056a.

STAR★METHODS

KEY RESOURCES TABLE

REAGENT or RESOURCE	SOURCE	IDENTIFIER
Chemicals, peptides, and recombinant proteins		
Polydimethylsiloxane (PDMS)	Dow Corning	Sylgard 184
Cyclohexane	Aladdin Reagent	C109819
1H,1H,2H,2H-perfluorooctyltriethoxysilane (97%)	Shanghai Dibo Biotechnology Co. Ltd.	SIC2266
graphene oxide (GO),50% wt.	Shanghai McLean Biochemical Technology Co. Ltd.	G10194
polyethylene terephthalate (PET)	Shanghai McLean Biochemical Technology Co. Ltd.	P82487
Software and algorithms		
visio	Microsoft	https://www.microsoft.com
Origin	OriginLab Corporation	https://www.originlab.com
Other		
scanning electron microscopy (SEM)	ZEISS	https://zeiss.com.cn
Energy dispersive spectrometer (EDS)	ZEISS	https://zeiss.com.cn
the LFA467 NanoFlash instrument	NETZSCH	https://analyzing-testing.netzsch.com/en
contact angle meter JC2000D	Shanghai Zhongchen Digital Technology Equipment Co., Ltd.	http://www.powereach.com/
Portable data logger	HIOKI, Japan	https://www.hioki.com/
solar simulator(CEL-PE300L-3A)	Beijing Zhongjiao Jinyuan Technology Co., Ltd.	http://www.bjaulight.com/

EXPERIMENTAL MODEL AND STUDY PARTICIPANT DETAILS

The model of this study is based on thermal conduction and fluid dynamics models.

METHOD DETAILS

Materials

Polydimethylsiloxane (PDMS), specifically Sylgard 184 base and curing agent, was purchased from Dow Corning. Cyclohexane (99.7%) was purchased from Aladdin Reagent. 1H,1H,2H,2H-perfluorooctyltriethoxysilane (97%) was purchased from Shanghai Dibo Biotechnology Co. Ltd. Candles were purchased from Taobao Boca Lighting Flagship Store. Commercially available 50% wt. graphene oxide (GO) paste, polyethylene terephthalate (PET) was purchased from Shanghai McLean Biochemical Technology Co. All remaining chemical reagents were provided by the laboratory and sterilized.

Preparation of the metamaterial

1. A 50% wt. graphene oxide (GO) slurry that is commercially available was diluted with ultrapure water to a final concentration of 20 mg/mL. The diluted GO suspension was then uniformly coated onto a polyethylene terephthalate (PET) substrate and evaporated at room temperature for 24 h to obtain a GO assembled film.
2. The metamaterial was subjected to annealing at 1300°C for 120 min, followed by annealing at 2850°C for 60 min in an argon (Ar) gas flow environment. The flexible gap was then obtained through a rolling process.
3. To create the dip coating solution, 0.5g of 1H,1H,2H,2H-perfluorooctyltriethoxysilane (PFOTES) was added to an 80 mL solution of cyclohexane and stirred magnetically for 2 h. Next, 1.5 g of PDMS and 0.15 g of curing agent were added to the mixed cyclohexane solution. The solution was dispersed by ultrasonic waves for 30 min and then stirred magnetically for 6 h. The photothermal superhydrophobic coating was obtained by immersing the graphene film, prepared using the redox method, into a solution at a rate of 0.03 m/s. The film was first placed at the two-thirds position of a candle flame to collect soot from incomplete combustion. The immersion-coated film was then vacuum-dried for 20 min. This process was repeated five times to achieve the desired coating (Figure S1).

Sample characterization

The morphology of the samples was characterized using scanning electron microscopy (SEM, ZEISS). Energy dispersive spectrometer (EDS) measurements were performed to determine the elemental content. The thermal conductivity of graphite film (GF) was measured using the

laser flash method in the LFA467 NanoFlash instrument according to standard test method ASTME1461. Contact angle (CA) and sliding angle (SA) were measured using 10 μL of deionized water droplets analyzed by a contact angle meter JC2000D (Shanghai Zhongchen Digital Technology Equipment Co., Ltd.). Solar thermal experiments were conducted using a solar simulator (CEL-PE300L-3A, Beijing, China). The experimental data collection uses a data acquisition instrument (HIOKI, Japan).The de-icing performance was investigated using a customized cryogenic test rig.

Performance evaluation

Photothermal conversion, photothermal de-icing/anti-icing, and electrothermal de-icing/anti-icing of the samples were determined using an in-house visualized experimental system. The temperature variations of the samples were tested at different OPDs and EPDs, respectively. The photothermal conversion performance of GPCS (Graphene films, PDMS and polymers with carbon nanoparticles), G (graphene film), and aluminum panels under one solar illumination condition was also compared and the temperature distribution on the sample surface was captured using an infrared thermal imager.

The delayed freezing time of individual droplets under different light intensities was measured to characterize the anti-icing properties of the material. A 10 μL droplet was first injected onto the surface of the sample material at room temperature, and then the humidity inside the refrigeration cavity was controlled to be about 35%. At this time, the water-cooled refrigeration system was turned on, and the temperature inside the cavity was rapidly reduced. Then the temperature controller was adjusted to −10°C, −20°C and −30°C to investigate the delayed freezing time of the droplets in three different temperature environments.

In addition, the materials were tested for de-icing/defrosting properties. Specifically, samples were placed on the surface of a water-cooled refrigeration sheet in an open environment. The refrigeration system was then switched on and the refrigeration rate was maintained at 2 °C/min until the surface temperature dropped to −20°C. After 1 h, a thin layer of frost was formed on the surface of the material, after which a xenon lamp was switched on to observe the defrosting behavior of the material under one sunlight. Then a layer of ice with a thickness of about 3 mm was prepared with a mold, placed on the surface of the material and the de-icing properties of the material were observed under one sunlight.

The mechanical durability properties of the prepared photothermal anti-icing/de-icing materials were tested by water flow impact and sand impact experiments, respectively. The mass of water flow and sand for each drop was fixed, and then the angular change of each drop was detected by contact angle and rolling angle gauges. The photothermal materials were also placed in an outdoor environment to test their durability performance in the outdoor environment.

QUANTIFICATION AND STATISTICAL ANALYSIS

Statistical analysis of data was performed using Excel (Microsoft) and Origin (OriginLab).